Effect of mobility ratio on interaction between the fingers in unstable growth processes

Agnieszka Budek,[1,2] Kamil Kwiatkowski,[1,3] and Piotr Szymczak[1]

[1]*Institute of Theoretical Physics, Faculty of Physics, University of Warsaw, Pasteura 5, 02-093 Warsaw, Poland*

[2]*Institute of Geophysics, Polish Academy of Science, Ksiecia Janusza 64, 00-681 Warsaw, Poland*

[3]*Interdisciplinary Centre for Mathematical and Computational Modelling, University of Warsaw, Prosta 69, 00-838 Warsaw, Poland*

(Received 21 March 2017; published 30 October 2017)

We investigate interactions between thin fingers formed as a result of an instability of an advancing front in growth processes. We show that the fingers can both attract and repel each other, depending on their lengths and the mobility ratio between the invading and displaced phase. To understand the origin of these interactions we introduce a simple resistor model of the fingers. The predictions of the model are then compared to the numerical simulations of two unstable growth processes: dissolution of partially cemented rock fracture and viscous fingering in a regular network of channels.

DOI: 10.1103/PhysRevE.96.042218

I. INTRODUCTION

Many physical processes involving moving boundaries produce fingering patterns. Well-known examples include viscous fingering [1–5], electrochemical deposition [6,7], growth of bacterial colonies [8–10], crystallization in supercooled liquids [11,12], or dissolution of porous medium [13–17]. In all of these processes, the advancing interface becomes unstable if the mobility of the invading phase is larger than that of a displaced phase. Small perturbations of the interface grow and transform into fingers, which compete for the fluxes which feed them. A paradigm of these processes is a (two-phase) Laplacian growth problem [18] known also as the Muskat problem [19], in which the fluxes are associated with the harmonic field. The equations governing the growth are then given by (cf. Fig. 1):

$$\nabla^2\Psi_1(\mathbf{x},t) = 0 \qquad \mathbf{x}\in\mathcal{D}_1, \tag{1}$$

$$\nabla^2\Psi_2(\mathbf{x},t) = 0 \qquad \mathbf{x}\in\mathcal{D}_2, \tag{2}$$

$$\Psi_1(\mathbf{x},t) = \Psi_2(\mathbf{x},t) \qquad \mathbf{x}\in\Gamma_t, \tag{3}$$

$$(\lambda_1\nabla\Psi_1(\mathbf{x},t))_n = (\lambda_2\nabla\Psi_2(\mathbf{x},t))_n \qquad \mathbf{x}\in\Gamma_t, \tag{4}$$

$$U_n(t) = \alpha(\lambda_2\nabla\Psi_2(\mathbf{x},t))_n \qquad \mathbf{x}\in\Gamma_t. \tag{5}$$

In the above, $\mathcal{D}_1$ denotes an invading phase, $\mathcal{D}_2$ denotes displaced phase, and Γ_t is an interface. Next, Ψ stands for the field which is driving the growth (e.g., pressure in viscous fingering or temperature in solidification). The associated flux is given by $J_i = \lambda_i\nabla\Psi_i$, where λ_i is a mobility of phase i. Both the field and the normal component of the flux are assumed to be continuous across the interface. Finally, Eq. (5) links the advancement velocity of the interface (U_n) and the flux, with α being a proportionality constant and subscript n denoting the component normal to Γ. We will assume the system to be (quasi-)two-dimensional.

Equations (1)–(5) should be supplemented with appropriate far-field boundary conditions, which depend on a particular geometry in which growth takes place. For rectangular geometry one usually imposes the condition of a uniform flux at infinity

$$\lim_{x\to-\infty}\lambda_1\nabla\Psi_1(\mathbf{x},t) = \mathbf{e}_x = \lim_{x\to\infty}\lambda_2\nabla\Psi_2(\mathbf{x},t), \tag{6}$$

where x is the flow direction.

An important dimensionless parameter characterizing the system is the mobility ratio, $M = \lambda_1/\lambda_2$. Whenever $\lambda_1 > \lambda_2$, the flux of the field over the crest of a small protrusion of the interface is larger than that in the surrounding flat regions and thus initially flat interface breaks into fingers. The aspect ratio of the fingers tends to increase in time, since the field gradient is always the largest at their tips. Finally, the fingers become stabilized by surface tension, kinetic undercooling, or other short-scale regularization mechanisms, which depend on a particular problem at hand.

Note that in the limit $M\to\infty$ the problem reduces to a classical, one-phase Laplacian growth, driven by one field only (Ψ_2) with the condition $\Psi_2 = 0$ imposed on the moving boundary.

The nonlinear stages of finger dynamics are strongly dependent on M. In the context of viscous fingering, already the experiments of Habermann [20] have shown that as M is increased the pattern becomes progressively irregular with a strong screening between the fingers, due to which the longer fingers suppress the growth of the shorter ones. Similar morphological changes of the fingering pattern with M have been found in numerical simulations [21–28]. The numerical approaches differed in the way that randomness is introduced in the system: either through quenched disorder or fluctuations. The first approach is taken, e.g., in the pore-network models of fluid displacement in porous media where the pore throat diameters are usually randomly distributed [26,28,29]. The second is the basis of various modifications of DLA algorithm, which take into account finite mobility of the invading phase [21–26,28]. One conclusion from these numerical studies is that low values of M correspond to more compact patterns. In fact, it has been conjectured that at any finite M there is a crossover between fractal and compact patterns in the limit of long time or small grid size. This hypothesis have subsequently been supported by the results of renormalization group approaches [30,31]. Using a different approach, Otto [32] has shown that the "fingering zone" in the rectangular geometry grows linearly in time, which is also consistent with its nonfractal character (see Fig. 2 for the definition of leading edge, trailing edge, and the fingering zone).

As noted by Sherwood [24] an important distinction between the finite and infinite M case is that in the former the interface between the two fluids continues to advance,

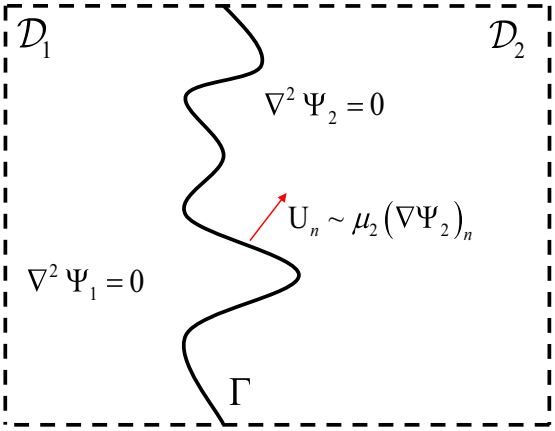

FIG. 1. A schematic of the system with an invading phase $\mathcal{D}_1$ and a displaced one $\mathcal{D}_2$. The interface, Γ moves with velocity U proportional to the field gradient.

albeit slowly, at points far behind the finger tips (trailing edge in Fig. 2). On a level of the interaction between the fingers this corresponds to the appearance of the stable fixed point in the phase space, in which the ratio of the growth velocities approaches a constant [33]. This corresponds to the incomplete screening, with the shorter fingers continuing to grow behind the front of the longer ones. This is the reason why the trailing edge moves with a finite speed, as predicted by a number of effective models [34–36]. The existence of the compact region filled entirely with the invading fluid has been nicely demonstrated in the experiments by Allen and Boger [37] as well as the recent studies by Bischofberger *et al.* [38,39]. The patterns reported in these papers provide a

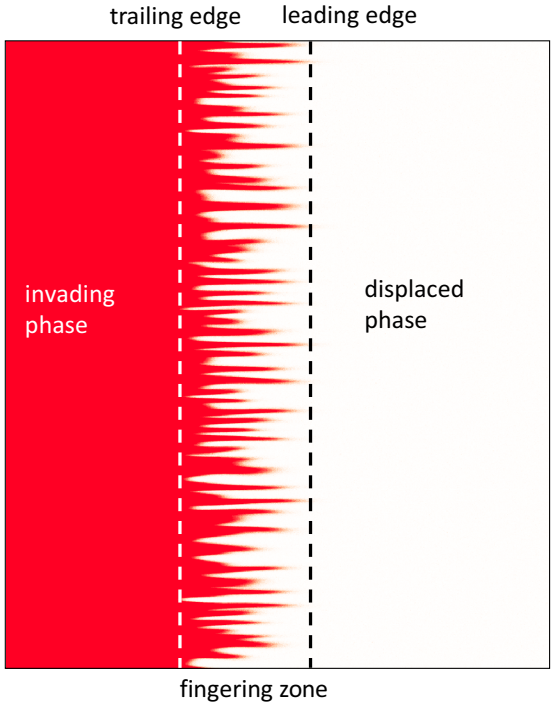

FIG. 2. Trailing edge marks the completely invaded area, while leading edge is defined by the tips of the most advanced fingers.

striking illustration of the impact of mobility contrast, showing a transition between ramified fingers and compact structures with a corrugated perimeter.

In this paper, we focus on a particular class of fingered growth systems, in which the emergent fingers are long and thin. Due to the high field gradients at their tips, these structures grow predominantly in length but not that much in diameter. Such structures are observed, e.g., in the electrochemical deposition experiments [6,40], smoldering combustion [41–43], side-branches growth in crystallization [11,12], evolution of seepage channel networks [44,45], wormholes forming in dissolving rocks [46], or anisotropic viscous fingers [29,33]. The two latter examples will serve to illustrate the theoretical findings in this paper.

Figure 3 illustrates the patterns in a dissolving fracture for different values of the mobility ratio, M. We describe this system in more detail in Sec. III A and in Appendix B, here we present the patterns in order to illustrate the characteristic features of the finger-finger interaction. As observed, there is a notable change in morphology as M is increased. For small M, the instability produces a chaotic sea of fingers incessantly merging, shielding, and fading. As M gets larger, the spacing between the fingers grows, and thus they become less prone to merging. Instead, shorter fingers get attracted to the base of the longer ones, which produces characteristic looped structures with the islands of the receding phase surrounded by the invaded one. Interestingly, the longest fingers are no longer attracted to each other but rather repel slightly, as observed in Fig. 3(b). With a further increase of M, we enter the hierarchical growth regime, where the fingers do not merge anymore, but instead grow straight and strongly compete for the flow. The longer fingers easily screen off the shorter ones in the neighborhood the size of which is of the same order as the finger length [13,47]. The process then repeats itself, which results in a distance between the active fingers increasing in time and eventually leads to the appearance of a scale-invariant, power-law distribution of finger lengths [47,48].

The central question that we address here is whether the structure of the pattern, such as that in Fig. 3 can be understood in terms of the interaction between the fingers. In many cases the answer to this question is positive. Krug *et al.* [49] have shown that the length distribution of Laplacian fingers in hierarchical growth regime (large M, right panel of Fig. 3) can be derived based on the estimate of the screening time in two-finger problem. Halsey and Leibig [50] derived the multifractal properties of DLA aggregates based on the analysis of the finger-finger interaction. However, the above studies assumed that the boundary between the phases is a potential isoline, which corresponds to the infinite mobility contrast between the phases. The present study, on the other hand, focuses on the impact of finite M values of the patterns. As we show, the character of the interaction between the fingers drastically changes as M is increased: from weak repulsion at small M values, through strong attraction at intermediate M back to the weak repulsion at large mobility contrasts.

The paper is organized as follows. In Sec. II a simple model of finger-finger interaction is introduced. In the model both the fingers of the invading phase as well as the regions of the displaced phase around them are represented as a collection of resistors of two different resistivities. The model is then applied

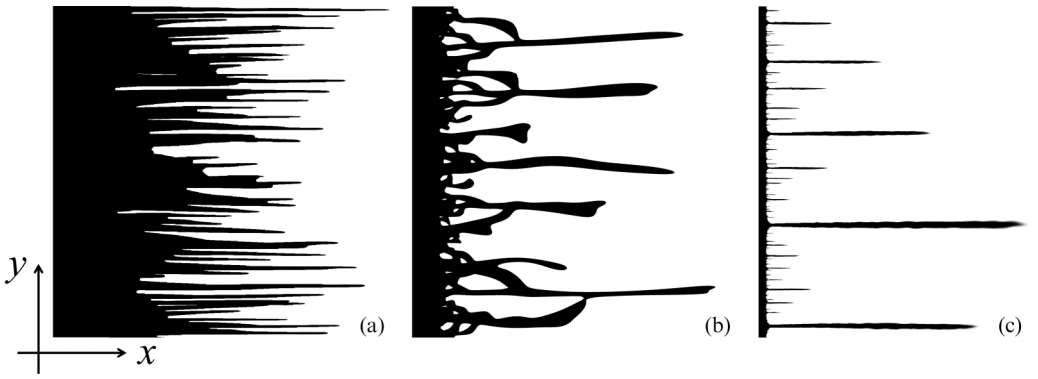

FIG. 3. Pattern formation in a dissolving fracture infiltrated by a reactive fluid, as described by Eqs. (B1)–(B5) of Appendix B. The dissolved region is marked in black. The dissolution proceeds in a highly nonuniform manner, with the formation of well-defined fingers in which both the fluid flow and reactant transport focus. The patterns corresponds to the mobility contrast of $M = 2$ (a), $M = 64$ (b), and $M = 1000$ (c).

in Sec. III to interpret the patterns formed in two systems. The first is a partially cemented rock fracture gradually dissolved by an acidic fluid. The second is the unstable infiltration of a more viscous fluid by a less viscous one in a regular network of channels. Finally, the conclusions are drawn in Sec. IV.

II. FINGER INTERACTION MODEL

As discussed in a preceding section, the fingers may attract, screen off, or repel one another, depending on their relative lengths as well as the value of the mobility ratio M. In order to understand the origins of this behavior we introduce a simple theoretical model where the system of growing fingers is mapped onto a resistor network.

In the model, we track the flow along the main routes in the system only. Since the highest pressure gradients are at the finger tips [51], we introduce lateral connectors between the fingers there, as shown in Fig. 4. The resistors represent either the invading phase (gray in Fig. 4, with resistivity ρ_1 per unit length) or the displaced phase (white in the figure, with resistivity ρ_2). The mobility contrast is then $M = \rho_2/\rho_1$.

To elucidate the mechanism of finger-finger interaction, we consider a paradigmatic setup with a longer finger (of length L) and a shorter one (of length l) in a periodic cell of width W, as illustrated in Fig. 4. The width of the cell can thus be interpreted as the average distance between the longest fingers in the system.

The shorter and longer finger are positioned asymmetrically in the cell, as otherwise they would continue to grow straight, without deflection, due to the symmetry. The distance between the fingers is assumed to be equal to one third of the cell width. Additionally, at a distance $W/3$ from both the shorter and the longer finger we introduce the line of resistors (EF) representing the undissolved matrix in the neighborhood of the fingers. The introduction of this element is the main difference between the present model and the one introduced in Ref. [52], where only the exchange of the flow between the fingers has been tracked. Constant pressures P_{in} and P_{out} are imposed at the inlet of the system, and on the line positioned at the distance L_{eq} from the tip of the long finger. The latter represents the distance at which pressure becomes uniform and the impact of the fingers is no longer felt. This distance increases as the pattern coarsens, being proportional to W. For large mobility contrasts, when the pressure drop along the finger can be neglected, L_{eq} can be calculated to be (see Appendix A)

$$L_{\text{eq}} = \frac{W}{2\pi}. \tag{7}$$

To keep the model simple, we assume that the hydraulic resistance is simply a product of resistor length and resistivity. Thus, for the configuration in Fig. 4 we have, e.g.,

$$R_{\text{AB}} = \rho_2 L_{\text{AB}}, \quad R_{\text{AC}} = \rho_1 L_{\text{AC}}, \ldots. \tag{8}$$

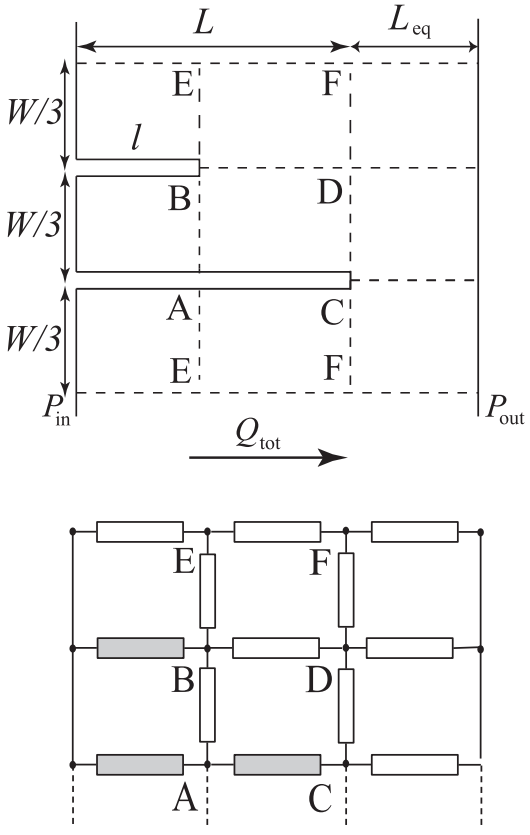

FIG. 4. The system consisting of two fingers (upper) and the corresponding resistor model (lower). Gray resistors, representing the finger of an invading phase, are of a smaller resistivity than white resistors (representing the displaced phase).

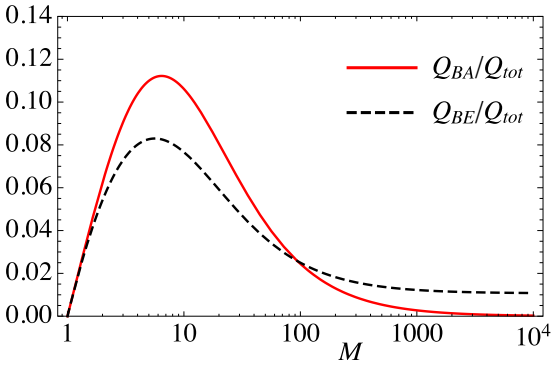

FIG. 5. Transverse flows at the tip of the shorter finger as a function of the mobility ratio M for $l/L = 0.3$ and $W/L = 0.3$ in the resistor model of Fig. 4. The flow Q_{BA} is marked by a solid line whereas Q_{BE} is dashed. The flows are normalized by the total flow in the system.

Here L_{AB} and L_{AC} are the distances between the points A and B and A and C, respectively. Next, given the constant pressure difference between the edges, the fluxes in the system can be calculated by straightforward algebra solving hydraulic equivalents of Kirchhoff's circuit rules.

The key parameter, determining the structure of the pattern, is the balance between the fluxes Q_{BE} and Q_{BA} at the tip of the shorter finger. If $Q_{\mathrm{BE}} > Q_{\mathrm{BA}}$, then the shorter finger directs itself away from the longer one, whereas if $Q_{\mathrm{BA}} > Q_{\mathrm{BE}}$ it gets attracted towards its companion. On the other hand, the ratios between the transverse fluxes (Q_{BA}, Q_{BE}) and the longitudinal one (Q_{BD}) determine the amount of the deflection of the finger trajectory.

Figure 5 shows the transverse fluxes at the tip of the shorter finger (normalized by the total flow in the system) as a function of the mobility contrast calculated using the resitor model of Fig. 4. Other parameters have been taken to be $W/L = 0.3$ and $l/L = 0.3$, which corresponds to the typical values characterizing the interaction between the fingers in Fig. 3(b).

As observed, at intermediate mobility contrasts the flow towards the longer finger (Q_{BA}) dominates over the flow away from it (Q_{BE}). Thus in this regime the shorter finger gets attracted to the longer one. At $M \approx 100$ the situation changes and the flow away from the finger begins to dominate—the shorter finger is then repelled from the longer one.

The transition point between these two behaviors depends on the length of the shorter finger as well as on the cell width. These two dependencies are characterized by the contour plots in Figs. 6 and 7, where we also mark the boundary between the region where attraction dominates ($Q_{\mathrm{BA}} > Q_{\mathrm{BE}}$) and that where the fingers repel each other. Figure 6 demonstrates that attraction is the strongest for intermediate M and l/L values whereas both for $l/L \approx 0$ and $l/L \approx 1$ repulsion dominates. A strong repulsion for equal-length fingers is to be expected—such fingers strive to reach a symmetric position in the cell, with the distance between them equal to $W/2$.

Figure 7, on the other hand, shows that magnitude of the interaction strongly depends on the aspect ratio of the periodic cell. Small W/L values correspond to the cases were the fingers are relatively close to each other. This enhances the finger-finger interaction, mostly attraction, which is at its strongest for $W/L \leqslant 0.3$. Larger distances between the fingers result invariably in repulsion, but the magnitude of this effect is quite small, quickly decreasing with W. The importance of aspect ratio of the system for the dynamics of the fingering front has been emphasized in a number of

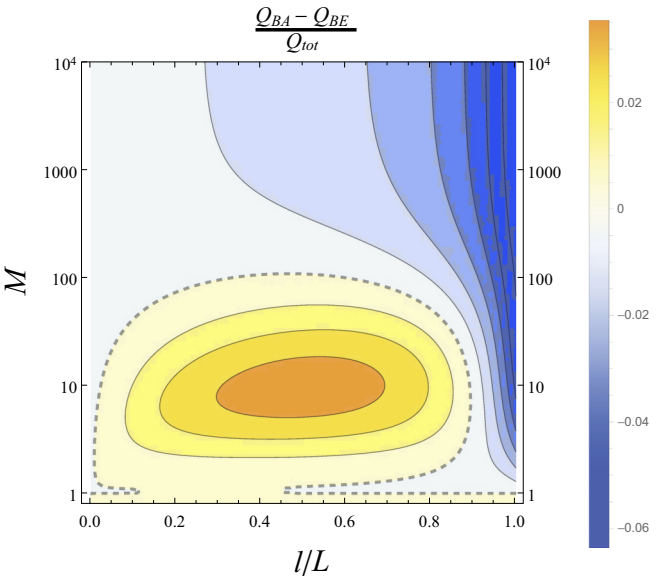

FIG. 6. Difference between transverse flows at the tip of the shorter finger as a function of the mobility ratio and the ratio of the lengths l/L for $W/L = 0.3$ in the resistor model of Fig. 4. The flows are normalized by the total flow in the system. The dashed line marks the boundary between the regions of attraction and repulsion between the fingers.

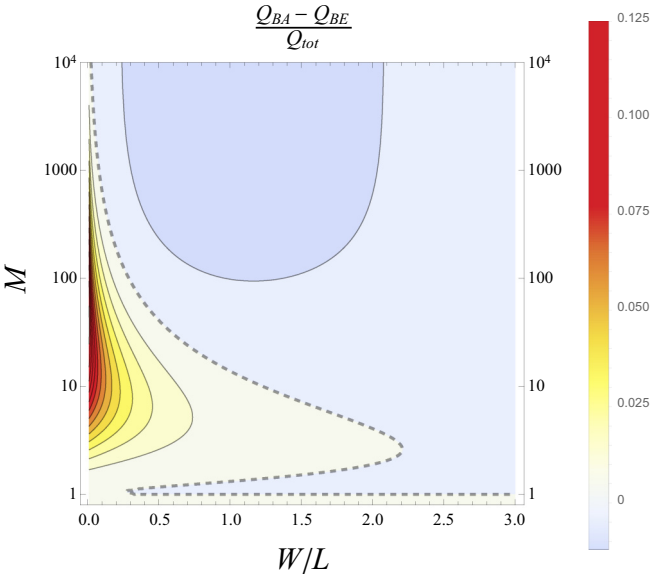

FIG. 7. Difference between transverse flows at the tip of the shorter finger as a function of the mobility ratio and the aspect ratio of the system W/L for $l/L = 0.3$ in the resistor model of Fig. 4. The flows are normalized by the total flow in the system. The dashed line marks the boundary between the regions of attraction and repulsion between the fingers.

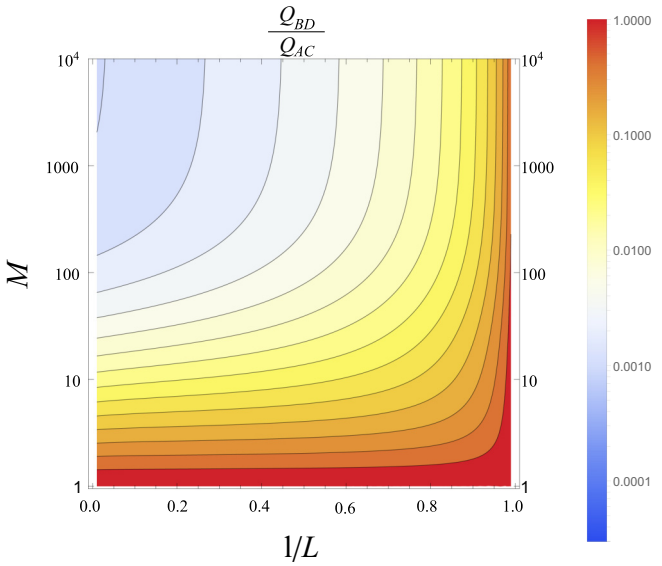

FIG. 8. Screening between the fingers: the ratio between the axial flow at the tip of the shorter finger to the flow in the longer one, $Q_{\mathrm{BD}}/Q_{\mathrm{AC}}$ (in the logarithmic scale).

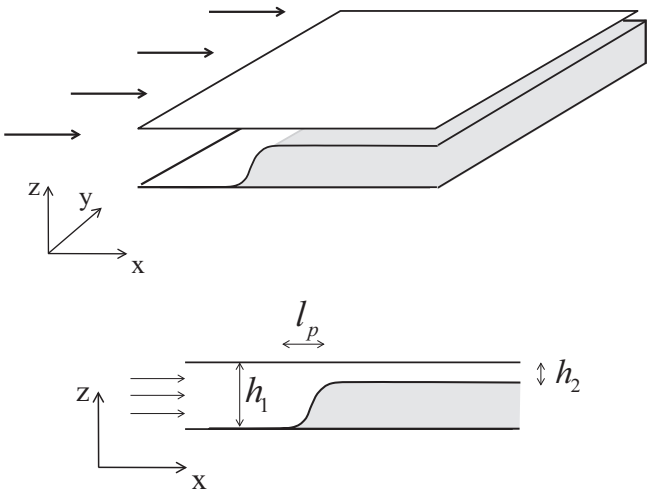

FIG. 9. A schematic view of a partially cemented fracture. The low-pH reactive fluid (marked by arrows) enters the fracture from the left-hand side and dissolves the carbonate cement (gray) located in between two inert walls. As a result, the initial aperture of the fracture (h_2) gets gradually enlarged until it reaches the value of h_1. The transition between h_1 and h_2 takes place over the length scale l_p, corresponding to the penetration length of the reactant (see the discussion in Appendix B).

studies [53–56]. In particular, Yang *et al.* [56] shown that the system behaves in a fundamentally different way in a small and large aspect ratio regime. Small aspect ratios lead to negligible transverse flows, and thus the system reduces to a collection of noncommunicating layers. Large aspect ratios, on the other hand, promote strong transverse flows and hence intensive mixing, which substantiates transverse averaging procedures proposed in a number of semiempirical approaches to the description of viscous fingering in porous media [34–36].

Notably, the results of our resistor model are in agreement with these observations. As observed in Fig. 7, for $W/L \gg 1$ (small aspect ratio) the transverse flows vanish and the fingers hardly interact with each other [as manifested by the fact that the parameter $(Q_{\mathrm{BA}} - Q_{\mathrm{BE}})/Q_{\mathrm{tot}} \to 0$]. This corresponds to noncommunicating layered system regime of Yang *et al.* [56]. On the other hand for large aspect ratio (small W/L) the interaction is very strong (distinct maximum in Fig. 7 for small values of W/L). Strong transverse flows in this regime lead to intense merging of the fingers and transverse mixing of the phases.

Finally, the present model can also be used to quantify the screening of the shorter finger by the longer one. This effect is measured by the ratio of the axial flow in the shorter finger, Q_{BD} to the flow in the longer finger, Q_{AC}. As observed in Fig. 8, the screening is at its strongest for large M and small to intermediate l/L. In fact, in the limit $M \to \infty$ the screening can be shown to be exponential [51], i.e., $Q_{\mathrm{BD}}/Q_{\mathrm{AC}} \sim e^{-(L-l)}$. As soon as M becomes finite, the exponential screening is replaced by a power-law one. The impact of finite mobility ratio on finger screening has also been analyzed in Ref. [57] by tracing the dynamics of a pair of the fingers in the coordinates corresponding to the ratio of their velocities and the ratio of the lengths. It has been shown that for finite M the stable fixed point of these dynamics is different from zero, which shows that the longer finger screens the shorter one only partially. The same is true for our system—even if $l \to 0$ the ratio of hydraulic resistances along the paths BD and AC remains finite, which results in the finite value of the growth velocity of the shorter finger in the long-time limit.

III. EXAMPLES: FRACTURE DISSOLUTION AND VISCOUS FINGERING

In this section we check the predictions of the finger interaction model against numerical simulations of two processes, which can be approximated with the two-phase Laplacian growth, Eqs. (1)–(5). The first is the dissolution of partially cemented rock fracture and the second is viscous fingering in a regular network of channels. What these systems have in common is that—as a result of an instability of the advancing front—well pronounced, large aspect ratio fingers are formed. Further evolution of the system is then controlled by the interaction between these fingers, the main features of which we aim to characterize using the resistor model.

A. Dissolution of partially cemented fractures

The first system that we consider is a partially cemented rock fracture flushed with a reactive fluid. The fluid, usually acidic, dissolves the cement, thus increasing the aperture of the fracture. A schematic view of such a system is presented in Fig. 9—the acidic solution, flowing from the left to the right, dissolves a layer of cement (marked in gray). The aperture of the fracture in the dissolved part (h_1) is thus larger than the aperture in the part which has not yet been dissolved (h_2). Note that the pattern in Fig. 3 correspond to the xy projection of the system, with the fully dissolved areas marked in black.

The details of the mathematical model of a dissolving fracture are given in Appendix B. As argued there, the volumetric flux of a thin film of liquid is well approximated

FIG. 10. Evolution of the dissolution patterns in a cemented fracture for $M = 100$. The columns correspond to four different moments of time when the pattern reaches 10%, 35%, 50%, 70%, and 100% of the total length of the system. The patterns have been obtained by solving Eqs. (B1)–(B5) of Appendix B.

by the Darcy law

$$\boldsymbol{q} = -\frac{h^3}{12\eta}\nabla p, \tag{9}$$

with the mobility proportional to the third power of the aperture. Thus in this case

$$M = \left(\frac{h_1}{h_2}\right)^3. \tag{10}$$

Such systems have been studied experimentally [58] but they are also of a practical importance. In some of the shale reservoirs the amount of carbonate cementation in the fractures is significant so that it hinders the exchange of the shale gas between the fracture and the matrix. Acidization of these fractures might be one of the possible ways of enhancing of the productivity of such reservoirs.

Let us now go back to Fig. 3, presenting the acidization patterns, to interpret it in the light of the results of the resistor model. First, we note that the strongest attraction takes place at intermediate M [Fig. 3(b)], but only for the finger pairs in which one finger is significantly shorter than the other one in full agreement with the predictions of the resistor model.

The appearance of the loops is a fingerprint of the attraction between the fingers. As shown in Fig. 11 the loops are abundant for mobility contrasts $M \in (10-100)$, i.e., precisely in the regime where the resistor model predicts the strongest attraction. Note a characteristic hierarchical structure of the loops, with the smaller ones nested within the larger ones. This implies self-similarity of a process: the width of the fundamental cell (W) increases in time along with the lengths and distances between the longest fingers. A finger initially regarded as a long one in our model system, may later be viewed as a short one when interacting with another, more distant neighbor.

Importantly, the character of the interactions between the fingers in Fig. 3(b) changes with their relative length—while shorter fingers are forming loops, the longer ones weakly repel each other, deflecting their trajectories to reach symmetric, equidistant positions in the cell. This is in accordance with Fig. 6, where attraction changes to repulsion at about $l/L \approx 0.6$. This effect can also be observed when analyzing the time evolution of the pattern (Fig. 10). At the beginning, when the length differences between the fingers are relatively small, the repulsion is a prevailing effect (cf. the second and third frames in Fig. 10). With time, however, as the length differentiation among the fingers increases, the longest ones start to attract their shorter neighbors and a nested loop structure is established.

On the other hand the patterns at small M [Fig. 3(a)] are rather uniform, without a strong differentiation between the fingers. There are two reasons for this: first, screening between the fingers is very weak at small M values, as shown in Figs. 6 and 7. Second, the characteristic distances between the longest fingers in the pattern are now much smaller than their lengths ($W/L \ll 1$), which, according to Fig. 7, leads to a weak repulsion only.

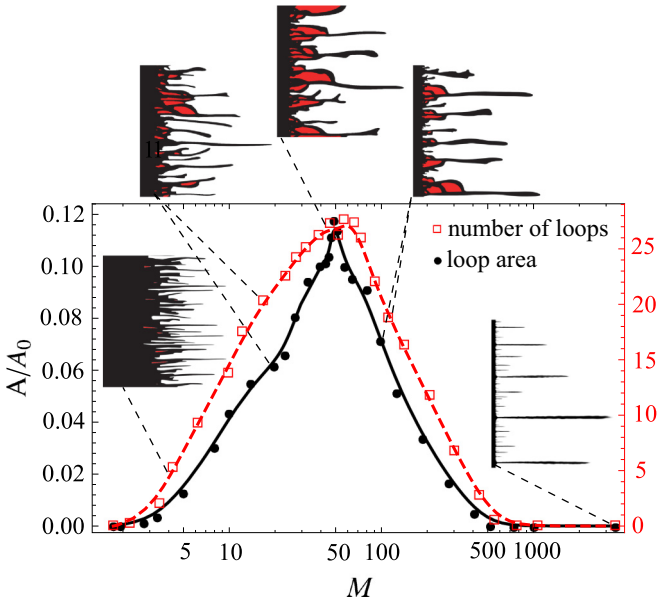

FIG. 11. The number of loops and the area covered by them in simulations of chemical erosion of partially cemented fractures, as described in Appendix B. The area covered by the loops (A) is normalized by the total area (A_0). Simulation results have been averaged over 16 realizations for each M.

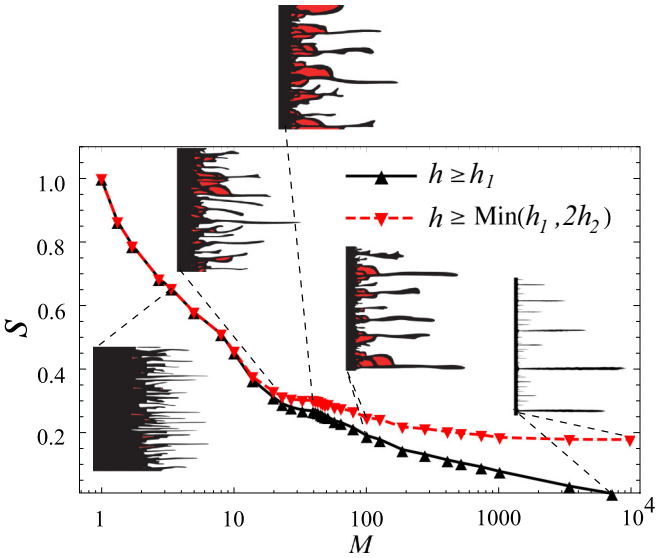

FIG. 12. Sweeping efficiency: fraction of the total area taken by the invading phase as a function of the mobility contrast for a dissolving fracture system. Two different criteria of being a part of a dissolved phase are used: either full dissolution ($h = h_1$) or twofold increase of an initial aperture ($h = 2h_2$).

Finally, at very large mobility contrasts [Fig. 3(c)] the patterns become strongly hierarchical, with the longest fingers almost completely screening the shorter ones within a distance equal to their length, in agreement with the prediction of the resitor model (cf. Fig. 8). On the other hand, according to Fig. 7, such aspect ratios of the unit cell ($W/L \approx 1$) combined with large M values should result in a very weak repulsion with only minimal deflection between the fingers.

An important quantity from a practical view point is the so-called sweeping efficiency, $s(M)$, which measures the percent of the invading phase in the system at breakthrough, i.e., the moment when the longest finger reaches the outflow. Large sweeping efficiencies are essential in engineering applications, e.g., when using the fluid displacement techniques to recover oil from the reservoirs [59]. In the case of partially cemented shale fractures, achieving large sweeping efficiencies is also important, since the main object here is to uncover as large area of the shale matrix as possible. As shown in Fig. 12 this is particularly easy to achieve if M is relatively small. Since $M = (h_1/h_2)^3$ this implies relatively small thickness of cement layers. As expected, at $M = 1$ the sweeping efficiency approaches one, since the boundary between the phases remains then planar and advances in a stable way. As M is increased, $s(M)$ gradually decreases, due to the increased differentiation in finger lengths due to the competition between the fingers. There is a plateau in $M(s)$ dependence near $M \approx 100$, i.e., in the loop formation regime. A closer inspection of the patterns in this regime shows that a significant amount of the fluid is then used for the dissolution of transverse connections between the fingers at the expense of a slower advancement of the longest fingers. To elucidate this, let us extend the model of Fig. 4 by allowing for a possibility of a partial dissolution of BA connector (inset of Fig. 13), which represents the situation during the loop closure. As shown in Fig. 13, closing of a loop is associated with a dramatic increase

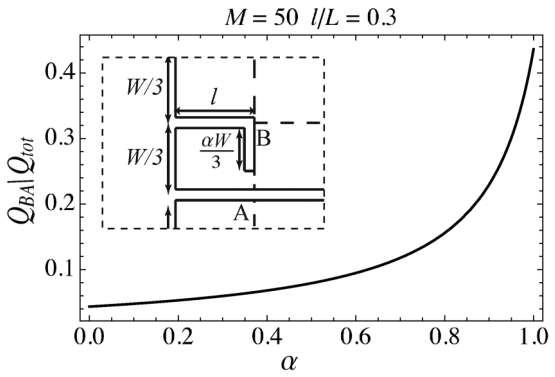

FIG. 13. Flow through the BA connector, normalized by the total flow, as a function of length of a dissolved part.

of Q_{BA} and the respective speedup of the dissolution rate of this connector—the loops are closed at an increasingly rapid pace. On the other hand, the total reactant flux supplied to the system is kept constant, hence also a total dissolved volume per unit time remains the same. The faster dissolution of transverse connectors must then result in a slowdown of the advancement of the fingers themselves.

There is a subtlety connected with the definition of invading and receding phase in a dissolved fracture system. As h_1 is increased with respect to h_2 it gets progressively longer to fully dissolve the cement layer and reach $h = h_1$. As a result, dissolution fingers might be reaching the outflow even before the layer gets fully dissolved anywhere in the system and the fully dissolved area no longer provides a good estimate of the extent of the pattern. As a result, there is certain ambiguity in the identification of a "dissolved" and "undissolved" phase at large h_1/h_2 ratios. In Fig. 12 we use two different criteria for a dissolved phase: either full dissolution ($h = h_1$) or a twofold increase of an initial aperture ($h = 2h_2$), the former more meaningful at small, the latter at large h_2/h_1 ratios. Within the first criterion $s(M)$ approaches zero for large M, since it becomes progressively harder to fully dissolve any given point in the system. The second criterion gives a finite sweeping efficiency at infinite M, similarly to the results for viscous fingering in a porous medium [20,23]. Let us note in this context that even the limit $h_1 \to \infty$ is physically realizable–it corresponds to the dissolution of a narrow fracture in a large block of completely soluble material (e.g., limestone rock), a classical problem in the studies of cave and karst formation [60–63].

B. Viscous fingering in a regular network

The second process considered in the present work is the displacement of a more viscous fluid by a less viscous one in a regular network of cylindrical pores (see Fig. 14). In classical experiments on the fluid displacement, performed in a Hele-Shaw cell, a multifinger growth regime is just a short transient, and soon the fingers coalesce into a single-finger final state. On the other hand, when the experiments are performed in a regular network of channels, a well-defined (and long-lived) fingers are formed, which then interact creating intricate patterns [29]. Due to anisotropy related to the presence of the network one obtains relatively thin fingers growing along

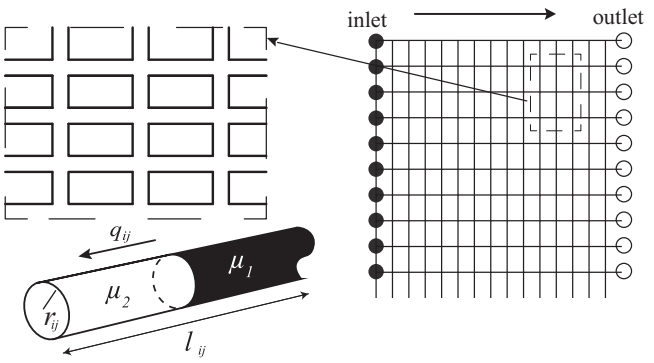

FIG. 14. Viscous fingering in a rectangular network of channels—schematic view. The network is initially filled with the fluid of high viscosity. Low viscosity fluid is then injected along the left hand side (dark circles) where constant pressure is imposed.

the flow direction. Transverse pores, on the other hand, are responsible for interactions between fingers. The details of the system together with a comprehensive analysis of its behavior are given in Refs. [57] and [29] and they are shortly summarized in Appendix C. Here we just mention that the equivalent of the Darcy law (9) is in this case given by a relation

$$\boldsymbol{q} = -\frac{\pi}{128\mu_i} d^4 \nabla p, \tag{11}$$

linking the volumetric flux in the pore, $\boldsymbol{q}$, with its diameter d. This time, the geometry of the system is not changing in time, but there is a viscosity difference between the invading and displaced phase. The mobility contrast is thus

$$M = \frac{\mu_2}{\mu_1}. \tag{12}$$

The time frames presenting the evolution of the system for different values of M are shown in Fig. 15. Again, the area occupied by the invading phase is marked in black while the displaced phase is left transparent. Even though the nature of this system is quite different from the dissolving fracture, many features of the patterns are shared across the two. For the largest mobility contrast ($M = 10^5$) a hierarchical pattern forms, due to a strong screening between the fingers. Initially, a large number of fingers are formed. However, as soon as the lengths of the fingers become comparable to the distance between them, the fingers begin to screen each other off. The strongest screening interactions arise between the neighboring fingers,

FIG. 15. Simulation results of viscous fingering in a rectangular network of pores for different mobility contrasts: $M = 10^5$ (lower row), $M = 100$ (center row), and $M = 5$ (upper row). The area occupied by a less viscous fluid is black while the rest of the system is transparent. The size of the network is 100×100. The columns correspond to four different moments of time when the pattern reaches 10%, 35%, 70%, and 100% of the total length of the system.

hence every second finger, on average, loses the competition and dies. The other half of the fingers continue to grow. Then, these longer fingers begin to interact with themselves, again screening each other off. This leads to the appearance of the self-affine pattern. The finger width is proportional to the flow through it and thus it tends to increase in time as the flow focuses in a decreasing number of active fingers. Apart from a strong screening between the fingers one can also observe a weak repulsion between fingers of similar length. This repulsive effect is manifested in an asymmetrical shape of neighboring fingers, with the invading fluid preferentially filling the transverse connectors in the direction away from the companion finger (see the red circle in Fig. 15).

The most interesting patterns are formed at intermediate mobility contrasts (cf. the center row in Fig. 15). Once again we observe a competition between fingers, however it is weaker than in a hierarchical regime, with more fingers reaching the outflow. What we see, on the other hand, is the appearance of transverse connections between the tips of the shorter fingers and their longer neighbors (cf. the red circle in the figure), which is equivalent to the loop formation in dissolving fractures, described in a preceding section. A more blocky, rectangular geometry of the loops here is the effect of an underlying lattice. Except for this, the appearance of the pattern is quite similar to that in a fracture [Fig. 3(b)].

At the other end of mobility spectrum, for $M = 5$ (upper row of Fig. 15), the pattern becomes much less ordered, again in full analogy to the dissolution patterns of Fig. 3(a). The differentiation of the finger lengths due to screening is now very weak, nevertheless some coarsening of the pattern in time is observed, mostly due to the merging of the neighboring fingers. Another well-visible effect is the appearance of the trailing front, marking the area fully invaded with the low-viscosity fluid. Due to the incomplete screening, this front is moving with a finite velocity, which results in relatively large sweeping efficiencies in this regime.

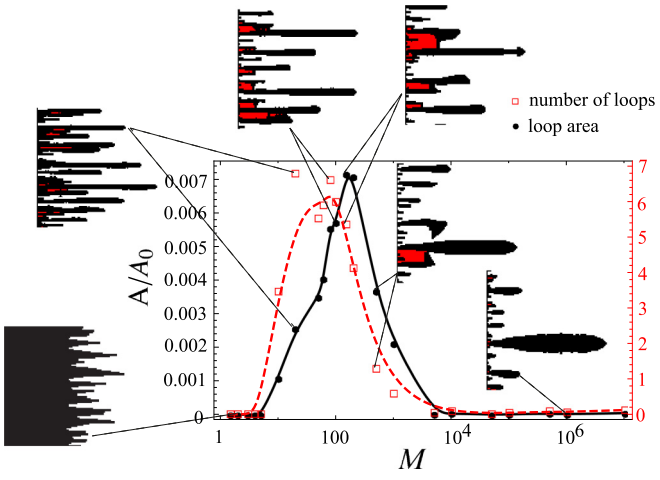

FIG. 16. Topology of fingers in simulations of viscous fingering in a rectangular network of channels. The area covered by loops is colored red. Loops smaller than five pores have not been taken into account. Simulation results have been averaged over 50 realizations for each M.

The dependence of the number of loops and areas covered by them on the mobility contrast is shown in Fig. 16. Once again, maximal loop formation occurs for $M \approx 50-100$. However, this time the maximum of loop area is shifted to the right with respect to the maximum in loop number: for smaller M loops are numerous but relatively small, whereas for larger M they become sparse but larger. Such a discrepancy between viscous fingering and chemical erosion patterns is a result of the fact that in the latter case merging between channels occurs more effectively than between viscous fingers and usually no material is left behind. The channels can, in general, grow at an arbitrary angles, while in viscous fingering systems only two directions were allowed. Thus the local maximum around $M \approx 10$ of Fig. 16 is not observed in Fig. 11, as the passage from merging toward attracting regime is more smooth.

IV. SUMMARY

Moving boundary problems, in which a more mobile phase invades a less mobile one, are characterized by a strong instability, which leads to the breakup of the initially planar front into fingers. These fingers either attract or repel each other, depending on their lengths, as well as the value of the mobility contrast between the phases.

We have shown that the mechanism of interaction between the fingers can be captured by a relatively simple resistor model, in which the key flowpaths in the system are represented in terms of resistors of two different resistivities, corresponding to the invading and displaced phase, respectively. The model predicts that a strong attraction between short fingers and their longer neighbors appears at intermediate mobility contrasts. This leads to the formation of characteristic loops, with the region of displaced phase surrounded by the invading one. Repulsion, on the other hand, is predicted to happen between equal-length fingers at large mobility contrasts. The fingers then deflect to reach an equidistant distribution within the sample.

The predictions of the resistor model are in a good agreement with the simulation results for two growth processes: dissolution of partially cemented rock fracture and viscous fingering in a regular network of channels. Remarkably, not only have we obtained a qualitative similarity, but also a close quantitative match: the model correctly predicted the region of maximum attraction to be in the range of ($M \approx 50-100$). Indeed, in this region, we have observed the most intense loop formation in both systems. Such an agreement shows that the mobility contrast is one of the main driving factors in the evolution of the patterns.

However, it is important to emphasize that the resistor model, although effective in predicting general features of the finger-finger interaction, is based on a highly simplified representation of the fingering pattern. The displaced phase is represented by a couple of resistors only, neglecting the transverse flow everywhere except at the finger tips. By using a constant resistivity per unit length we are also not taking into account the effects connected with nonuniform width of the fingers. Next, we neglected interfacial effects, such as surface tension, and other short-distance regularization mechanisms. These are present in the model only implicitly, as they control the characteristic width of the fingers.

Finally, the paradigmatic Laplacian growth problem (1)–(5) is in itself an idealization, and the two growth processes considered here depart from it in a number of details. They also differ between themselves: in a number of fields involved (pressure in the viscous fingering vs. pressure, reactant concentration and aperture in the dissolving fracture) as well as in short-distance regularizations and anisotropy effects (surface tension and grid effects in viscous fingering vs. the effects of finite penetration length in the fracture). Clearly, all these details do influence the fingering patterns, as can be appreciated by comparing Fig. 3 with Fig. 15. When contemplating all of these effects, it may seem striking that the relatively simple resistor model works so well. We hypothesize that the success of the model lies in two facts. First, in all cases pressure is the main field responsible for the interaction between the fingers. Even though there are two more fields (reactant concentration and aperture) involved in a fracture problem, in the undissolved region between the fingers concentration vanishes and the aperture is simply constant ($h = h_1$), thus the fingers communicate via the pressure field only. Second, as argued elsewhere [33,52] the highest pressure gradients and largest transverse flows are at the tips of the fingers, hence the resistor elements placed there can indeed capture most of the finger-finger interaction.

ACKNOWLEDGMENTS

This work was supported by the SHALESEQ project, funded by the Polish-Norwegian Research Programme operated by the National Centre for Research and Development (Poland) under the Norwegian Financial Mechanism 2009-2014 (Contract No. POL-NOR/234198/100/2014).

APPENDIX A: DERIVATION OF THE EQUILIBRATION LENGTH

In this Appendix we derive Eq. (7) for the length over which the pressure outside of the fingers becomes uniform. The derivation proceeds in the large M limit, in which the fingers can be assumed to be the equipotential lines. The Laplacian field around such fingers can be obtained using conformal mapping techniques. We start with the periodic array of fingers in the complex plane extending from $(-\infty, Wik)$ to $(0, Wik)$ with $k \in \mathbb{Z}$ (see Fig. 17). These represent the longest fingers in our system, with the distance of W between them.

We note that the mapping $\omega(z) = e^{\pi z/W}$ maps the region outside of the fingers on an area outside the line segment $(-1,1)$. Additional mapping, $\xi(\omega) = \omega + \sqrt{\omega^2 - 1}$ maps this area on a region outside a unit circle in a complex plane. The solution of the Laplace equation vanishing on a circle is simply $\Psi(\xi) = \alpha \mathrm{Re} \log \xi$. Taking this back to original variables we recover

$$\Psi(x,y) = \frac{\alpha \pi x}{W} + \alpha \mathrm{Re} \log \left[1 + \sqrt{1 - e^{-\frac{2\pi}{W}(x+iy)}}\right]. \quad \text{(A1)}$$

The constant α can be fixed by requiring that $\partial_x \Psi \to 1$ as $x \to \infty$. This yields $\alpha = W/\pi$ and

$$\Psi(x,y) = x + \frac{W}{\pi} \mathrm{Re} \log \left[1 + \sqrt{1 - e^{-\frac{2\pi}{W}(x+iy)}}\right]. \quad \text{(A2)}$$

The first, y independent term describes uniformly raising pressure with the isolines parallel to y axis. The second term is a nonuniformity caused by the presence of the fingers. The characteristic scale over which this term becomes negligible is $L_{\mathrm{eq}} = W/2\pi$, which gives the result of (7).

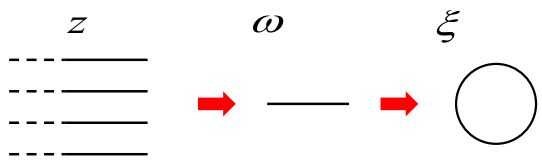

FIG. 17. Illustration of the composition of conformal maps described in the text.

APPENDIX B: DISSOLUTION OF CEMENTED FRACTURES

Here we summarize the mathematical model of a dissolving, partially cemented rock fracture. A schematic view of such a system is presented in Fig. 9—the acidic solution, flowing from the left to the right, dissolves a layer of cement (marked in gray) positioned in between two inert (insoluble) walls. The aperture of the fracture in the dissolved part (h_1) is thus larger than the aperture in the part which has not yet been dissolved (h_2).

The aperture of the fracture is usually orders of magnitude smaller than its lateral dimensions, thus the system can be considered as quasi-two-dimensional. This is exploited by introducing depth-averaged equations of mass, momentum, and solute conservation, which are obtained by averaging of the Stokes equation and convection-diffusion equation over the aperture [61,64,65]. Fluid flow is then described by the Reynolds equation for the local volume flux (per unit length across the fracture), $\mathbf{q}(x,y,t) = \int_0^h \mathbf{v}(x,y,z,t)dz$

$$\mathbf{q}(x,y,t) = -\frac{h^3(x,y,t)}{12\mu} \nabla p(x,y,t), \quad \nabla \cdot \mathbf{q}(x,y,t) = 0, \quad \text{(B1)}$$

where h is the aperture of the fracture, p is the pressure and μ is the fluid viscosity. The transport of hydrogen ions in the aqueous phase is described in terms of flow-averaged concentration field, $\tilde{c}(x,y) = \frac{1}{q(x,y)} \int_0^h v(x,y,z)c(x,y,z)dz$, with the 2D transport equation of the form

$$\nabla \cdot (\boldsymbol{q}\tilde{c} - Dh\nabla \tilde{c}) = -R, \quad \text{(B2)}$$

where ∇ is a two-dimensional (2D) (x,y) gradient operator, D is the diffusion coefficient and R is the sink term related to the dissolution of carbonate lamina by the acidic solution. For small pH the dissolution kinetics is well approximated be a simple one-step reaction [66]:

$$\mathrm{CaCO_3} + \mathrm{H^+} \to \mathrm{Ca^{2+}} + \mathrm{HCO_3^-}. \quad \text{(B3)}$$

with the calcite dissolution rate much faster than the rate of diffusive transport of $\mathrm{H^+}$ ions to the fracture surface (transport-limited regime). In this case, the reaction rate is transport-controlled and can be approximated by [65]

$$R(c) = \frac{D\mathrm{Sh}}{2h} c\theta(h_1 - h), \quad \text{(B4)}$$

where Sh = 7.54 is the Sherwood number for parallel plate geometry and θ is the Heaviside step function which guarantees that the reaction term vanishes in the region where all of the cement has dissolved (which corresponds to the aperture $h = h_1$). In this region Eq. (B2) reduces to a convection-diffusion equation.

Finally, we have an equation for the aperture increase due to the dissolution of cement

$$c_{\mathrm{sol}}\frac{\partial h(x,y,t)}{\partial t} = \frac{D\mathrm{Sh}}{2h}c\theta(h_1 - h), \tag{B5}$$

where c_{sol} is the molar concentration of the solid phase ($CaCO_3$). Note that, since $c_{\mathrm{sol}} \gg c$, the characteristic time scale of the cement dissolution is much longer than the timescale of ion concentration relaxation, which allows the time dependence in (B2) to be neglected [67,68].

There is a pressure drop Δp imposed between the two ends of the system, tuned in such a way as to keep the average flow rate in the fracture (q_0) constant. Additionally, at the inlet ($x = 0$) the acid concentration is set to a constant value of $c(x = 0, y) = c_0$. Downstream of the front the reactant concentration eventually vanishes, while the flow velocity becomes y independent.

Importantly—as illustrated in Fig. 9—the aperture profile in a dissolving fracture is changing smoothly between h_1 and h_2. The extent of such a partially dissolved region is related to the reactant penetration length (l_p in Fig. 9). The dimensional analysis gives

$$l_p \sim \frac{qh_2}{D\mathrm{Sh}}. \tag{B6}$$

For the two-phase approximation to work, this length should be smaller than other lengthscales characterizing the pattern, such as the lateral extent of the fingers. Due to the smallness of the aperture of the typical fracture, this condition holds except at the neighbourhood of the tips of the fingers, where the flow rates (q) can be exceedingly large.

The results of the simulations presented in Figs. 3 and 10 are obtained for the system of the size $4096h_2 \times 4096h_2$. The aperture-scale Péclet number, $\mathrm{Pe} = q_0/D$ has been set at 100. Several different lamina thicknesses has been considered, corresponding to different mobility contrasts, $M = (h_1/h_2)^3$.

APPENDIX C: VISCOUS FINGERING IN A RECTANGULAR NETWORK OF CHANNELS

The second system considered here is the displacement of a more viscous fluid by a less viscous one in a regular, planar network of cylindrical pores (see Fig. 14).

The mathematical model of this system is based on the assumption that the fluid flow in each elementary channel is governed by the Hagen-Poiseuille equation

$$q_{ij} = -\frac{\pi}{8\mu l_{ij}} r_{ij}^4 \Delta p_{ij}, \tag{C1}$$

where $\Delta p_{ij} = (p_j - p_i)$ denotes pressure drop along the channel joining node i with node j, q_{ij} is the volumetric flux in this channel, l_{ij} and r_{ij} stand for its length and radius respectively. Combining the above with the continuity condition

$$\sum_i q_{ij} = 0, \tag{C2}$$

allows one to find the pressures and flows in the network for single phase flow. Note that in the above we neglect the pressure drops associated with the nodes themselves.

When there are two phases in the elementary channel, we need to take into account the surface tension effects on the interface. Assuming that the invading fluid fills uniformly a given portion of the channel [of length $l_{ij}^{(1)}$], whereas the rest of the channel [i.e., $l_{ij}^{(2)} = l_{ij} - l_{ij}^{(1)}$] is filled with the displaced fluid (cf. Fig. 14), we get for q_{ij}

$$q_{ij} = \pm\frac{\pi}{8}\frac{1}{\mu_1 l_{ij}^{(1)} + \mu_2\left(l_{ij} - l_{ij}^{(1)}\right)} r_{ij}^4 \mathrm{Max}\left[|p_j - p_i| - \frac{2\sigma}{r_{ij}}, 0\right], \tag{C3}$$

where the indices 1 and 2 are used to denote the invading and displaced fluid, σ is the interfacial tension between the fluids and the sign depends on the direction of the pressure drop. Together, Eqs. (C2) and (C3) are the hydraulic equivalents of Kirchhoff's circuit rules, and constitute the basic equations of pore-network models of porous media [69]. This system of equations is solved iteratively for pressure values at all nodes. Based on these, the flow rates are calculated, and then the interface between the fluid is moved with the velocity corresponding to the mean flow rate in the capillary, i.e., $v_i = \frac{q_i}{\pi r_{ij}^2}$. The model presented above has been verified by comparison with microfluidic experiments [29] yielding good qualitative and quantitative agreement.

The simulations have been performed on a system of 100×100 elementary channels. The geometry of the system was anisotropic—the transverse channels (to the direction of the pressure gradient) were twice shorter than the longitudinal channels. On the other hand, the cross-sectional area of the transverse channels was larger than that of longitudinal channels, again by a factor of two. Such a geometry resulted in strong interactions between the viscous fingers. A detailed study of the impact of network geometry on the fingering patterns can be found in Ref. [29].

[1] S. Hill, Chem. Eng. Sci. **1**, 247 (1952).
[2] P. G. Saffman and G. Taylor, Proc. Roy. Soc. Lond. A **245**, 312 (1958).
[3] R. A. Wooding, J. Fluid. Mech. **39**, 477 (1969).
[4] L. Paterson, J. Fluid. Mech. **113**, 513 (1981).
[5] G. Homsy, Annu. Rev. Fluid Mech. **19**, 271 (1987).
[6] A. Kuhn and F. Argoul, Phys. Rev. E **49**, 4298 (1994).
[7] P. Meakin, *Fractals, Scaling and Growth Far from Equilibrium* (Cambridge University Press, Cambridge, 1998).

[8] I. Golding, Y. Kozlovsky, I. Cohen, and E. Ben-Jacob, Physica A **260**, 510 (1998).
[9] E. Ben-Jacob, H. Shmueli, O. Shochet, and A. Tenenbaum, Physica A **187**, 378 (1992).
[10] E. Ben-Jacob, I. Cohen, and D. Gutnick, Annu. Rev. Microbiol. **52**, 779 (1998).
[11] Y. Couder, F. Argoul, A. Arnéodo, J. Maurer, and M. Rabaud, Phys. Rev. A **42**, 3499 (1990).
[12] Y. Couder, J. Maurer, R. González-Cinca, and A. Hernández-Machado, Phys. Rev. E **71**, 031602 (2005).
[13] M. L. Hoefner and H. S. Fogler, AIChE J. **34**, 45 (1988).
[14] C. N. Fredd and H. S. Fogler, AIChE J. **44**, 1933 (1998).
[15] G. Daccord, Phys. Rev. Lett. **58**, 479 (1987).
[16] G. Daccord and R. Lenormand, Nature **325**, 41 (1987).
[17] F. Golfier, C. Zarcone, B. Bazin, R. Lenormand, D. Lasseux, and M. Quintard, J. Fluid Mech. **457**, 213 (2002).
[18] S. D. Howison, J. Fluid. Mech. **409**, 243 (2000).
[19] M. Muskat, *Flow of Homogeneous Fluids through Porous Media* (McGraw–Hill, New York, 1937).
[20] B. Habermann, Trans. AIME **219**, 264 (1960).
[21] M. J. King and H. Scher, Phys. Rev. A **41**, 874 (1990).
[22] M. Sahimi and Y. C. Yortsos, Phys. Rev. A **32**, 3762 (1985).
[23] A. DeGregoria, Phys. Fluids **28**, 2933 (1985).
[24] J. Sherwood and J. Nittmann, J. de Phys. **47**, 15 (1986).
[25] J. Sherwood, J. Phys. A: Math. Gen. **19**, L195 (1986).
[26] M. Blunt and P. King, Phys. Rev. A **37**, 3935 (1988).
[27] M. Ferer, R. A. Geisbrecht, W. N. Sams, and D. H. Smith, Phys. Rev. A **45**, R6973 (1992).
[28] M. Ferer, W. N. Sams, R. A. Geisbrecht, and D. H. Smith, Phys. Rev. E **47**, 2713 (1993).
[29] A. Budek, P. Garstecki, A. Samborski, and P. Szymczak, Phys. Fluids **27**, 112109 (2015).
[30] T. Nagatani and H. E. Stanley, Phys. Rev. A **41**, 3263 (1990).
[31] J. Lee, A. Coniglio, and H. E. Stanley, Phys. Rev. A **41**, 4589 (1990).
[32] F. Otto, SIAM J. Appl. Math. **57**, 982 (1997).
[33] M. Pecelerowicz, A. Budek, and P. Szymczak, Europhys. Lett. **108**, 14001 (2014).
[34] E. Koval, Soc. Petrol. Eng. J. **3**, 145 (1963).
[35] M. J. Todd and W. Longstaff, J. Pet. Tech. **24**, 874 (1972).
[36] F. J. Fayers, Soc. Pet. Engs. Reserv. Eng. **3**, 551 (1988).
[37] E. Allen and D. V. Boger, in *SPE Annual Technical Conference and Exhibition, 2–5 October 1988, Houston, Texas*, Vol. SPE 18097 (Society of Petroleum Engineers, 1988).
[38] I. Bischofberger, R. Ramachandran, and S. R. Nagel, Nat. Commun. **5**, 5265 (2014).
[39] I. Bischofberger, R. Ramachandran, and S. R. Nagel, Soft Matter **11**, 7428 (2015).
[40] P. Meakin, Phys. Rev. A **37**, 2644 (1988).
[41] O. Zik, Z. Olami, and E. Moses, Phys. Rev. Lett. **81**, 3868 (1998).
[42] O. Zik and E. Moses, Phys. Rev. E **60**, 518 (1999).
[43] C. Lu and Y. C. Yortsos, Phys. Rev. E **72**, 036201 (2005).
[44] O. Devauchelle, A. P. Petroff, H. F. Seybold, and D. H. Rothman, Proc. Natl. Acad. Sci. USA **109**, 20832 (2012).
[45] Y. Cohen, O. Devauchelle, H. F. Seybold, R. Yi, P. Szymczak, and D. H. Rothman, Proc. Natl. Acad. Sci. USA **112**, 14132 (2015).
[46] P. Szymczak and A. J. C. Ladd, J. Geophys. Res. **114**, B06203 (2009).
[47] V. K. Upadhyay, P. Szymczak, and A. Ladd, J. Geophys. Res.: Solid Earth **120**, 6102 (2015).
[48] A. Budek and P. Szymczak, Phys. Rev. E **86**, 056318 (2012).
[49] P. M. J. Krug, K. Kassner and F. Family, Eurphys. Lett. **24**, 527 (1993).
[50] T. C. Halsey and M. Leibig, Phys. Rev. A **46**, 7793 (1992).
[51] T. Gubiec and P. Szymczak, Phys. Rev. E **77**, 041602 (2008).
[52] P. Szymczak and A. J. C. Ladd, Geophys. Res. Lett. **33**, L05401 (2006).
[53] L. W. Lake, *Enhanced Oil Recovery* (Prentice Hall, Englewood Cliffs, NJ, 1989).
[54] Y. C. Yortsos, Transport Porous Med. **18**, 107 (1995).
[55] Z. Yang and Y. C. Yortsos, SPE J. **3**, 285 (1998).
[56] Z. M. Yang, Y. C. Yortsos, and D. Salin, Adv. Water Resour. **25**, 885 (2002).
[57] M. Pecelerowicz, A. Budek, and P. Szymczak, Eur. Phys. J. Spec. Top. **223**, 1895 (2014).
[58] F. Osselin, P. Kondratiuk, A. Budek, O. Cybulski, P. Garstecki, and P. Szymczak, Geophys. Res. Lett. **43**, 6907 (2016).
[59] N. Ezekwe, *Petroleum Reservoir Engineering Practice* (Pearson Education, Boston, 2010).
[60] W. Dreybrodt, Water Resourc. Res. **98**, 639 (1990).
[61] R. B. Hanna and H. Rajaram, Water Resourc. Res. **34**, 2843 (1998).
[62] W. Cheung and H. Rajaram, Geophys. Res. Lett. **29**, 2075 (2002).
[63] P. Szymczak and A. J. C. Ladd, Earth Planet. Sci. Lett. **301**, 424 (2011).
[64] R. L. Detwiler and H. Rajaram, Water Resourc. Res. **43**, W04403 (2007).
[65] P. Szymczak and A. J. C. Ladd, Geophys. Res. Lett. **40**, 3036 (2013).
[66] S. L. Brantley, J. D. Kubicki, and A. F. White, *Kinetics of Water-Rock Interaction* (Springer, Berlin, 2008).
[67] J. Chadam, D. Hoff, E. Merino, P. Ortoleva, and A. Sen, IMA J. Appl. Math. **36**, 207 (1986).
[68] A. J. C. Ladd and P. Szymczak, Water Resour. Res. **53**, 2419 (2017).
[69] M. J. Blunt, Curr. Opin. Coll. Int. Sci. **6**, 197 (2001).